Coupled Scattering and Reflection Measurements in Shallow Water

Charles W. Holland

***Abstract*—The characteristics of shallow-water reverberation are often controlled by scattering from the seabed. While scattering mechanisms are understood in general, the state-of-the-art falls far short of predicting the correct angular and frequency dependence of scattering in a given region. A series of acoustic and supporting geoacoustic measurements were conducted over a large area in the Straits of Sicily in order to study seabed scattering in a complex littoral environment. The hypothesis was that exploiting direct path reflection coefficient measurements, in conjunction with the scattering measurements, could help illuminate the underlying scattering mechanisms. The sediment at the seabed interface was found to be a fine silty clay with nearly uniform properties across the area. Notwithstanding this spatial homogeneity, 1–6-kHz reflection and scattering measurements showed significant spatial variability. The coupled reflection-scattering approach resolved this apparent discrepancy, revealing that the reflection and scattering processes are largely controlled by the sediment properties below, rather than at, the water sediment interface. Measurements at 3600 Hz show that site-to-site variability is in part controlled by the thickness of the silty-clay layer. Layers up to 10 m below the water sediment interface contribute to the scattering at 3600 Hz.**

***Index Terms*—Geoacoustic inversion, seafloor reflection, seafloor scattering, shallow-water acoustics.**

I. Background and Objectives

OVER THE past decades, a variety of physics-based seabed scattering models have been developed (e.g., [1]–[8]). These models require increasingly detailed geoacoustic properties of the seabed. For example, the incident field on the subbottom volume or interfaces can be predicted only if the deterministic background properties of the sediment column are known. Thus, analysis of scattering measurements require a substantial amount of geoacoustic information, and the modeler is nearly always in the position of having too little geoacoustic data.

The type of geoacoustic measurements that can be conducted depends in part upon the water depth (e.g., if divers can deploy equipment), and the scattering measurement technique itself (e.g., the size of the area involved in the scattering process and thus the size of the area that needs to be surveyed). In addition to state-of-the-art geoacoustic measurement techniques, it is proposed that reflection measurements can substantially augment geoacoustic data required for bottom scatter modeling. The results in [7] demonstrated in a deep-water environment that reflection measurements could be exploited to obtain key geoacoustic properties including sound speed gradients, density, attenuation, and layer statistics.

Following that approach, coupled measurements of seabed reflection and scattering have been made at shallow-water sites in the Straits of Sicily (see Fig. 1). By coupled, it is meant that the measurements are not only co-located, but sample commensurate spatial scales of the seabed. It is also meant that the processing and analyses employ commensurate assumptions and modeling. Finally, the analyses provide mutually beneficial information about the seabed interface and subbottom structure. The coupled approach also leads naturally to a self-consistent description of the sediment geoacoustic properties. A self-consistent geoacoustic description capable of predicting both reflection and scattering is an important goal in the development of seabed databases.

The measurements presented here were undertaken in an attempt to understand the bottom interaction process in a regional setting rather than at a single site. While it may be possible to fit a parameterized model for a given site, it is usually not clear how those parameters vary around the site, or even if the parameters capture the physical mechanisms or are simply proxies that adequately fit that data set. The coupled nature of the measurements and analysis with the Malta Plateau data illuminates several physical processes on a regional scale: 1) on the Malta Plateau the scattering arises principally from subbottom layers, rather than the water–sediment interface and 2) distinctness in the scattering strength from the various sites may be largely due to geometrical factors (i.e., layer thickness) rather than spatial variability in the scattering properties of the sediment. The fact that spatial variability can be linked to identifiable, deterministic processes fulfilled one of the goals of the study.

The paper is organized in the following manner. First, the experiment locations and general environment of the Malta Plateau are described. Then the reflection measurements are discussed, highlighting the geoacoustic properties that can be extracted from these data that are crucial for understanding (modeling) the scattering. Scattering measurements are then described and model-to-data predictions are provided which indicate the potential of the coupled approach. Conclusions regarding the data and methods are provided in the final section.

II. Environmental Data

In [9] the Straits of Sicily are described as "a geologically complex area dominated by microplates jostling amidst collision zone mountain belts forming between the African Craton and Europe." The experimental area (see Fig. 1) can be divided into two physiographic regions: the Ragusa Ridge, a lineated rocky outcrop forming a spine between Sicily and Malta

Manuscript received April 2, 2001; revised December 21, 2001. This work was supported by the NATO SACLANT Undersea Research Centre and the Office of Naval Research.

The author was with SACLANT Undersea Research Centre, 19138 La Spezia, Italy. He is now with the Applied Research Laboratory, Pennsylvania State University, State College, PA 16804 USA (e-mail: cwh10@psu.edu).

Publisher Item Identifier S 0364-9059(02)06316-1.

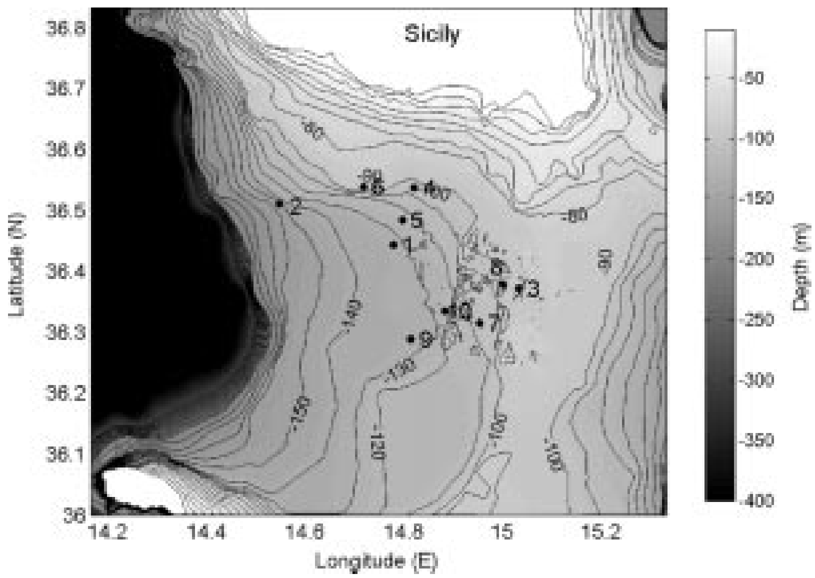

Fig. 1. Bathymetry (in meters) and site locations in the Straits of Sicily. The area bounded (roughly) by the 200-m contour is referred to as the Malta Plateau. The Maltese island of Gozo is in the bottom left corner of the plot.

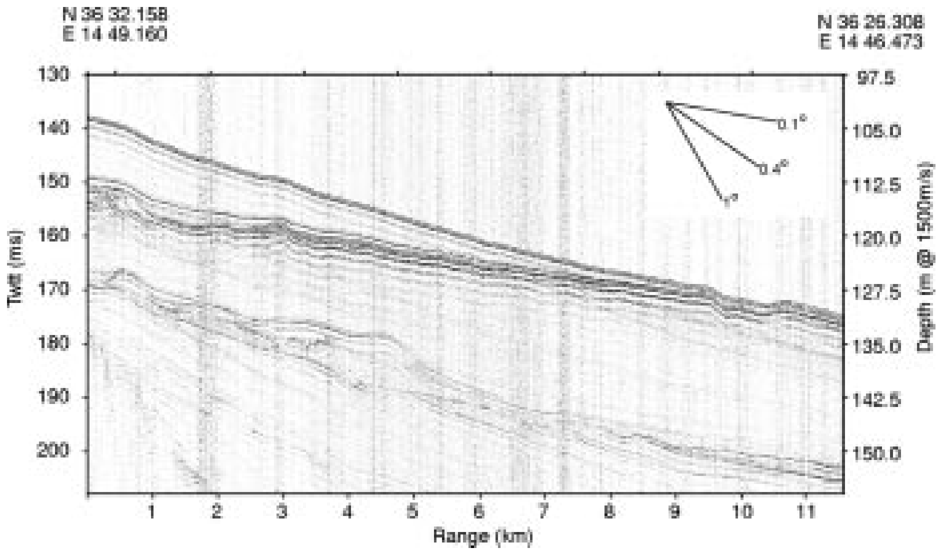

Fig. 2. Seismic reflection data of transect from Site 4 (0 km) to Site 1 (11 km). Site 5 is at 6.25 km. The vertical exaggeration is 100 : 1 and the inset shows the apparent slopes. Note that the angles of all the reflecting horizons are less than 1 degree. The base of the first sediment layer can be seen at Site 4 (0 km) at 150 ms two-way travel time (Twtt).

(roughly defined by depths shallower than ~110 m) and the area west of the Ragusa Ridge, termed the Malta Plateau. Nearly the entire area of the Malta Plateau is covered with a high-porosity silty-clay sediment, although a few areas in the northern region (e.g., near Site 6) exhibit rock outcrops. In this paper, reflection and scattering data sites on the Malta Plateau (Sites 1, 4 and 10) will be discussed. Acoustic and supporting geoacoustic measurements were conducted between 1998–2000.

Seismic reflection data from Site 4 to Site 1 are shown in Fig. 2. Note that the seafloor is smooth and flat, with slopes of the water–sediment interface and subbottom horizons much less than 1 degree. At Site 4, the first sediment layer is about 10 m thick and thins seaward.

In addition to seismic reflection data, sidescan, bottom video, piston (8 m barrel) core and gravity (1.3 m barrel designed to minimize sediment disturbance) core data were also collected. The gravity cores were stored upright; piston cores were sectioned into 4-m sections and stored horizontally after capping. During a geophysical survey conducted during May 1999, sound speed measurements were conducted at 200 kHz on the gravity cores (Sites 1 and 4) shortly after collection. However, problems in system calibration prevented measurement of absolute sound speed. Density measurements were made on piston cores in the laboratory following the cruise. The density measurements on the piston cores are believed to be biased due to the core settling and disturbance during transport which effects both the depth registration and density values. For the silty-clay sediments, the measurements are believed to represent an upper bound to the *in situ* values. Sound speed and density measurements made on gravity cores collected at Site 10 in April 2000 were made immediately following the core collection and are believed to be of high quality.

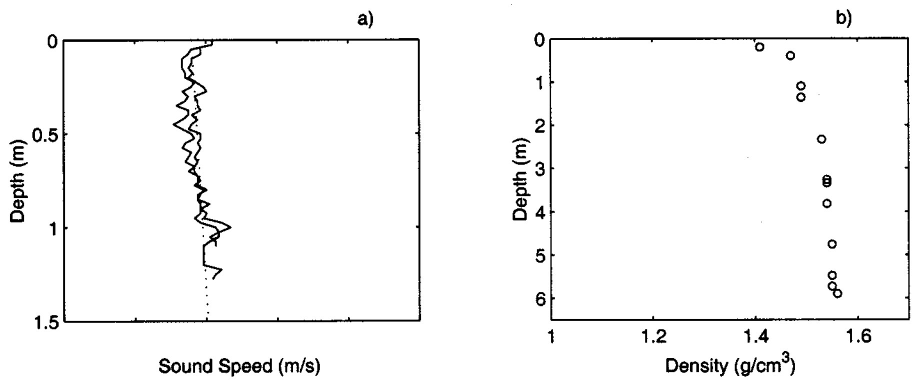

Fig. 3. Core measurements at Site 4 from: (a) two gravity cores separated by ∼60 m (the tick marks are at 10-m/s intervals and the dashed line is a sound speed gradient of 1.5 s^{-1}) and (b) a piston core.

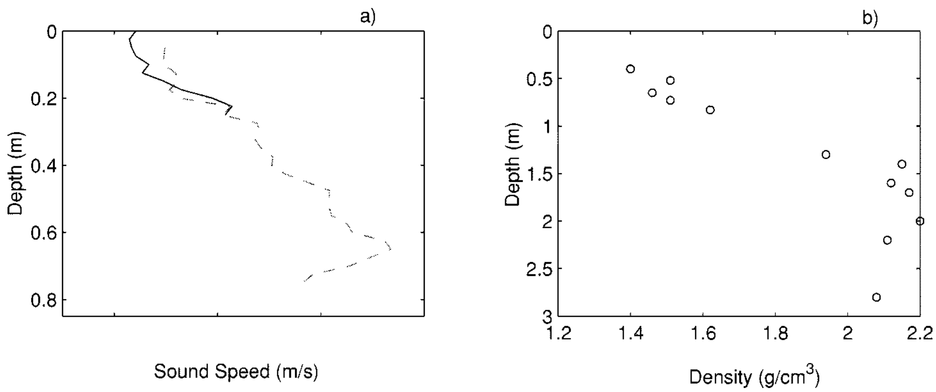

Fig. 4. Core measurements at Site 1 from: (a) two gravity cores separated by ∼20 m (the tick marks are at 20 m/s intervals) and (b) a piston core.

A. Site 4

The water depth at Site 4 is 102 m with a slight (∼0.2 degree) seaward slope. Sidescan and bottom video recordings show that the seafloor is featureless except for centimeter-scale holes from biologics. Three cores were collected that all contained a very homogeneous soft silty clay. Sound speed measurements (uncalibrated) on the gravity cores show a 1.5-s^{-1} gradient [Fig. 3(a)]. Density measurements on the piston core [Fig. 3(b)] are believed to represent an upper bound to the *in situ* density.

B. Site 1

Site 1 lies at 128-m water depth with a slight (∼0.1 degree) seaward slope. Sidescan data in this area shows a generally featureless bottom with faint lineations caused by dragnet fishing. Gravity coring at this site showed a silty-clay layer with a high sound speed gradient [see Fig. 4(a)]. Piston coring showed that below the silty clay layer there exists a thin sandy layer and then a pebble/shell layer extending for 2 m to the bottom of the core [Fig. 4(b)]. Fig. 5 is a photograph of the material found in the core catcher (about 3 m subbottom) and reasonably representative of the lower 2 m.

C. Site 10

The water depth at Site 10 is 125 m and the bathymetry is flat. The core data at Site 10 showed an upper layer (∼25 cm) of silty-clay, then a layer of clayey sand with shell fragments (∼30 cm), then gravelly sand. Fig. 6 provides the sound speed and density measurements.

Fig. 5. Photograph of contents in the core catcher at Site 1, showing large whole shells, shell fragments, pebbles, and cemented rock, in a muddy shelly gravel matrix. The coin in the foreground is 2.5 cm in diameter.

III. Reflection Measurements

A. Overview of Measurement and Inversion Techniques

The reflection technique was developed in order to extract high resolution (resolving layers of order 50 cm), geoacoustic information from the seabed [10]. The measurement technique and inversion strategy are briefly reviewed here.

The measurement configuration uses a broadband source and a single hydrophone (see Fig. 7). It is a "local" technique in the sense that it samples a relatively small (a few hundred me-

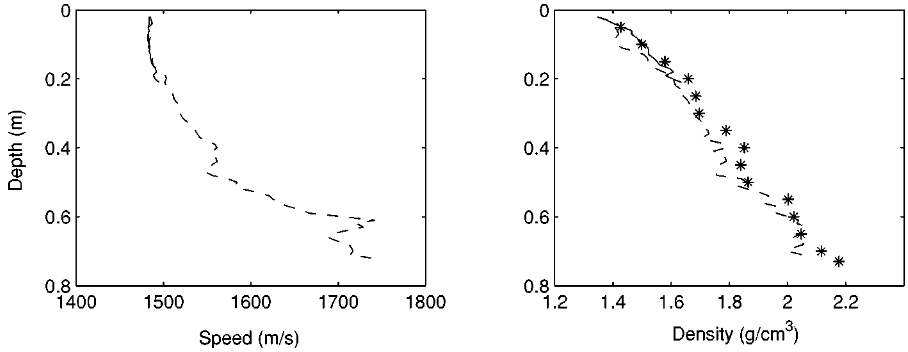

Fig. 6. Two gravity core analyses (solid and dashed lines) at Site 10 from the multisensor core logger. The asterisks were measured using standard laboratory methods as a cross check. The cores were separated by approximately 130 m.

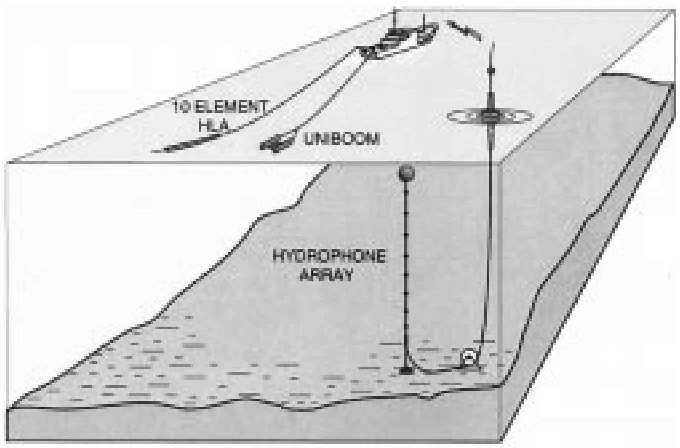

Fig. 7. Reflection experiment geometry. The data presented in this section are from a single hydrophone of the vertical array.

ters) region of the seafloor. This "local" attribute provides the opportunity to develop range-dependent geoacoustic models by making measurements at several sites (see [11]). The source employed in the experiments was either an EG&G Model 265 Uniboom (Site 4) or a Geoacoustics Model 5813B Boomer (Site 1) mounted on a catamaran at a nominal depth of 0.40 m. The usable bandwidth of the pulse is roughly from 0.5 to 10 kHz and the source repetition rate was 1 pulse per second. The receiver consisted of a vertical array of which only the bottom hydrophone ($\sim$15 m above the bottom) was employed in the analysis. Although multiple phones could be used to increase the data coverage, the data from one hydrophone is sufficient to meet the analysis requirements. Data were sampled at 48 kHz with a lowpass filter of 16 kHz and telemetered back to R/V Alliance.

Geoacoustic inversion schemes in general suffer from two main problems: 1) uniqueness, i.e., many diverse geoacoustic models can be made to fit the same data and 2) lack of an initial parameterization (e.g., determination of number of important sediment layers). The inversion strategy used in this paper extracts geoacoustic information from both the space–time domain as well as the space–frequency domain. The motivation for using data in both domains is to increase the amount of independent data (i.e., reduce uniqueness problems). In addition, the time-domain data provides a very useful initial parameterization. A third reason is that certain geoacoustic parameters may be best extracted in one domain. For example, density and attenuation are best extracted in the frequency domain, while layer thickness is best extracted in the time domain.

The inversion technique employed here follows a two-step process:

1) Time-domain data is used to obtain an initial parameterization (i.e., determine the number of layers in the seabed) and to provide initial estimates of the layer thickness and interval velocity for each layer.
2) Frequency-domain data (reflection coefficient) are used to refine the velocity structure and extract the density and attenuation. An important feature of the analysis is that the processing is performed in a layer-stripping approach. That is, first the reflection coefficient is obtained at just the water sediment interface, and the geoacoustic parameters for that interface are obtained. Next, holding those properties constant, the reflection coefficient for the first two sediment layers is processed and the geoacoustic properties extracted and so forth. The advantage of this technique over the traditional method of computing the total energy reflection coefficient is that it further increases the amount of independent data and thus further reduces uniqueness problems.

Additional details regarding the experiment design, data processing, and inversion can be found in [10].

B. Site 4 Reflection Analysis

Raw broadband time series data at Site 4 collected during the SCARAB98 experiment are shown in Fig. 8; the track was parallel to the bathymetric contours. The vertices of the hyperbolae are at the minimum offset between source and receiver, which in this case is 13 m. The earliest arrival is the direct path, then a group of four arrivals are visible that are reflections from bottom and subbottom layers. The last group of arrivals, having a minimum travel time of about 0.2 s, correspond to the second bottom bounce.

The shapes of the hyperbolas are a function of the geometry of the experiment and the sound speed structure. Knowing the geometry, the sound speed structure can be estimated using the ray parameter method [12]. In order to better visualize the data (in particular the bottom reflected paths) the data are mapped to reduced time, t_r, defined as

$$t_r^2 = t^2 - (r/c_r)^2$$

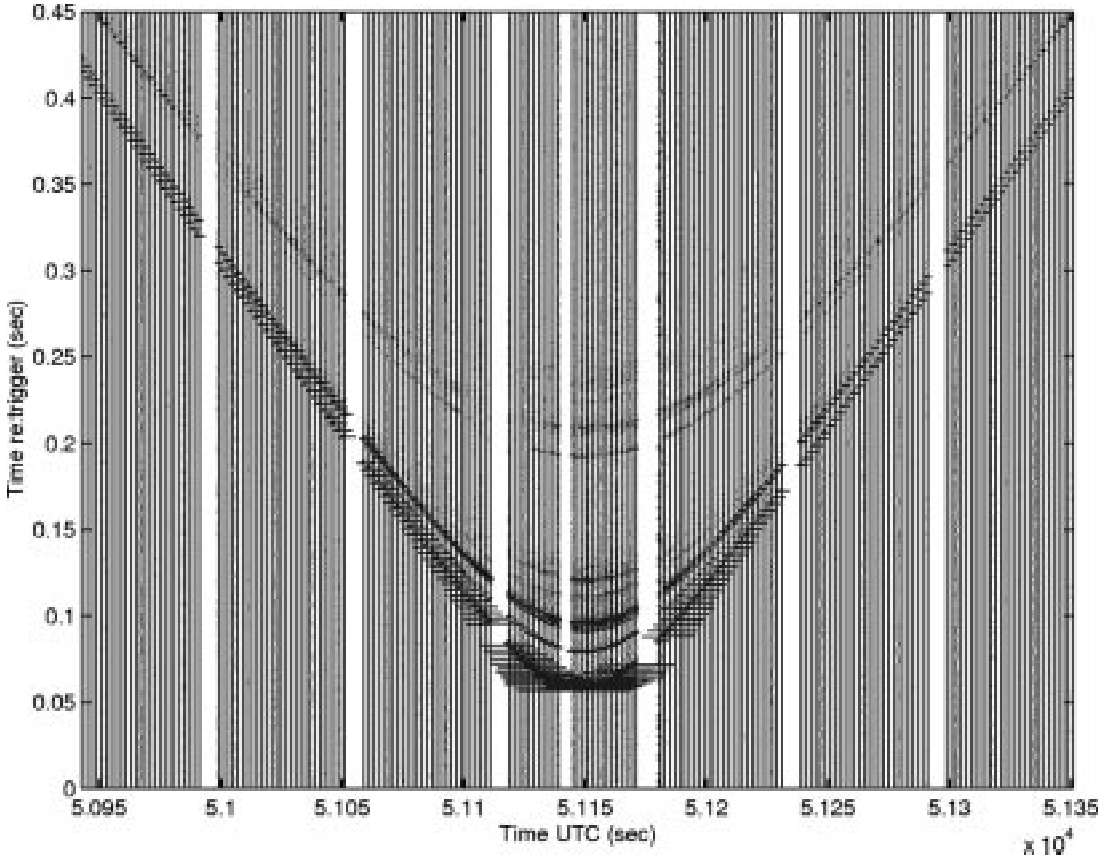

Fig. 8. Raw reflection time series data at Site 4.

where t is time, r is horizontal range, and c_r is the reducing velocity. Thus, arrivals traversing a path with an average velocity equal to that of the reducing velocity would be "flat" in range (i.e., independent of reduced time). In the transformed data (Fig. 9), the first reflection arrival at 0.0062 s^2 is from the water–sediment interface, later arrivals correspond to subbottom layers.

Also in this figure are the "picks" (dashed line) for each layer with the resulting interval velocity and thickness structure provided in Fig. 10(a). The "picks" are reflection arrivals that are selected interactively. Extensive tests using the method on synthetic data [13] show minimum errors associated with a ray parameter corresponding to $\sim$50° at the seabed and when a maximum offset[1] of $\sim$400 m is used to estimate stacking velocities. Errors associated with multilayer synthetic model inversions were less than 25 cm in depth estimates and less than about 1% in sound speed. Other errors are associated with geoacoustic properties that may vary in range (the technique assumes that the properties vary in depth only). Range dependence in the sediment properties is difficult to estimate, but in these environments it is believed to be small because the region of the seafloor probed is small (less than 60 m for the maximum offset of 400 m), several cores taken tens of meters apart showed no substantial variability, and the seismic data exhibit no apparent range dependence in reflectivity over this aperture. The small layer dips are very small, $\sim$0.06 degrees and lead to the slight asymmetry around zero range observed in Fig. 9. Assuming a zero dip results in an error of $\sim$0.7 m/s.

Between the first and third reflecting horizon there is a strong reflection (at $\sim$0.008 s^2) which corresponds to 8.4 m subbottom. Although the strength of the reflection indicates a strong impedance change at the boundary, the interval velocities on each side of the boundary were essentially identical. The simplest explanation is that there is a thin (smaller than the resolution of the pulse) layer interbedded in an otherwise homogeneous layer. The geoacoustic properties of this layer and the layer at 10 m subbottom ($\sim$0.009 s^2) cannot be extracted using the time-domain method but will be extracted using the frequency-domain data (reflection loss).

Processed reflection loss (defined as $-20\log_{10}|R|$, where R is the pressure reflection coefficient) data for the water–sediment interface (i.e., windowing around just the first arrival of Fig. 9) are shown in Fig. 11. One of the salient features of these data is that the water–sediment interface is nearly acoustically transparent; above grazing angles of 10 degrees, 99% of the energy is transmitted into the sediment. Thus, the subbottom sediment structure will tend to govern the reflection and scattering characteristics. The other salient feature in the data is the presence of the angle of intromission, the angle where the reflection coefficient approaches zero. The angle of intromission occurs when the sound speed ratio is less than 1 (see Fig. 10) and the density ratio is greater than 1.

[1]Another source of error is due to the fact that the hyperbola is an approximate, not exact representation of the arrival structure for reflection from a general layered media. For the geometry of this problem, 400 m was a compromise between having enough range extent to adequately characterize the arrival structure and a short enough range so that the hyperbolic assumption for the arrival time was robust.

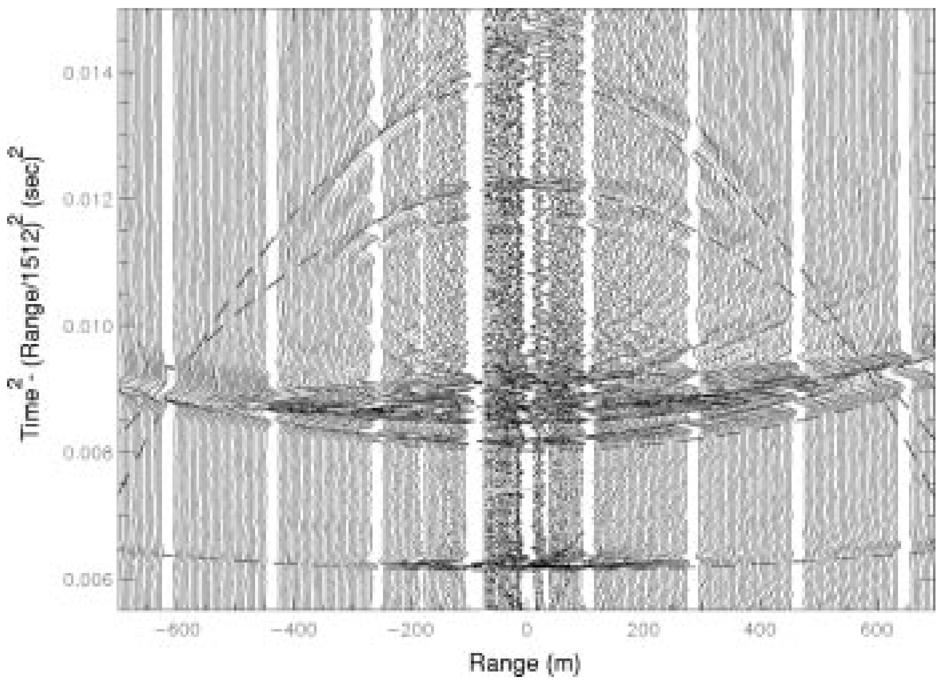

Fig. 9. Site 4 reflection data with horizon picks (dashed hyperbolas). The reflection from the water–sediment interface is at about 0.006 s^2.

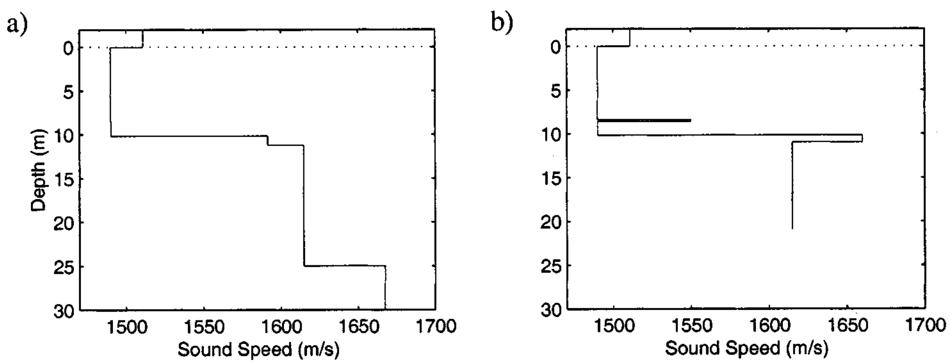

Fig. 10. Site 4 sediment sound speed from a time-domain analysis: (a) using hyperbolic fits to the main reflecting horizons and (b) the modified profile after frequency-domain analysis.

Generally, at this point in the analysis, the interval velocity obtained above would be used as a first estimate for the modeled reflection coefficient. However, in this case, the presence of the angle of intromission (δ) along with a measure of near-normal incidence reflection loss (υ) permits both the sediment velocity, c_2, and density, ρ_2, to be obtained unambiguously as

$$\rho_2 = \rho_1(1 - 4\upsilon/(\cos\delta(1+\upsilon))^2)^{-1/2} \quad (1)$$

$$c_2 = (\rho_1 c_1/\rho_2)(1+\upsilon)/(1-\upsilon). \quad (2)$$

The bottom water sound speed and density are 1511 m/s and 1.029 g/cm^3, respectively, yielding the sediment properties 1480 $\pm$ 4 m/s and 1.32 $\pm$ 0.04 g/cm^3 (see [14] which describes the inversion process in detail). The time-domain method yielded 1490 m/s averaged over the upper 10 m (see Fig. 10) and, using the gradient from the core data (see Fig. 3), a sediment-interface estimate of 1482.5 m/s is obtained which is quite consistent with the value obtained from the angle of intromission.

In a homogeneous material, the peak of the reflection loss at the angle of intromission is controlled by the intrinsic attenuation. However, interface roughness, fine-scale layering, and volume inhomogeneities in marine sediments can also control the small but finite loss at that angle. Since these latter effects are not known, only an "effective" attenuation can be extracted; this forms an upper bound to the intrinsic attenuation. Model-to-data comparisons using the inversion results are shown in Fig. 11 with a fitted effective attenuation of 0.07 dB/m/kHz. While that value is consistent with the work in [15], there is mounting evidence that Hamilton's estimates for fine-grained sediments are an order of magnitude too high (see [16]–[18] and [7]).

The model predictions of Fig. 11 are frequency-independent. Note that the fit between the model and the data are excellent from 800 to 2000 Hz, but above 2000 Hz the data show a dependence on frequency. The frequency dependence of the data is indicative of the presence of fine-scale layering and/or volume inhomogeneities. Modeling (see the Appendix) indicates that fine-scale layering is the main cause of the frequency dependence. The presence of fine-scale layering also explains the re-

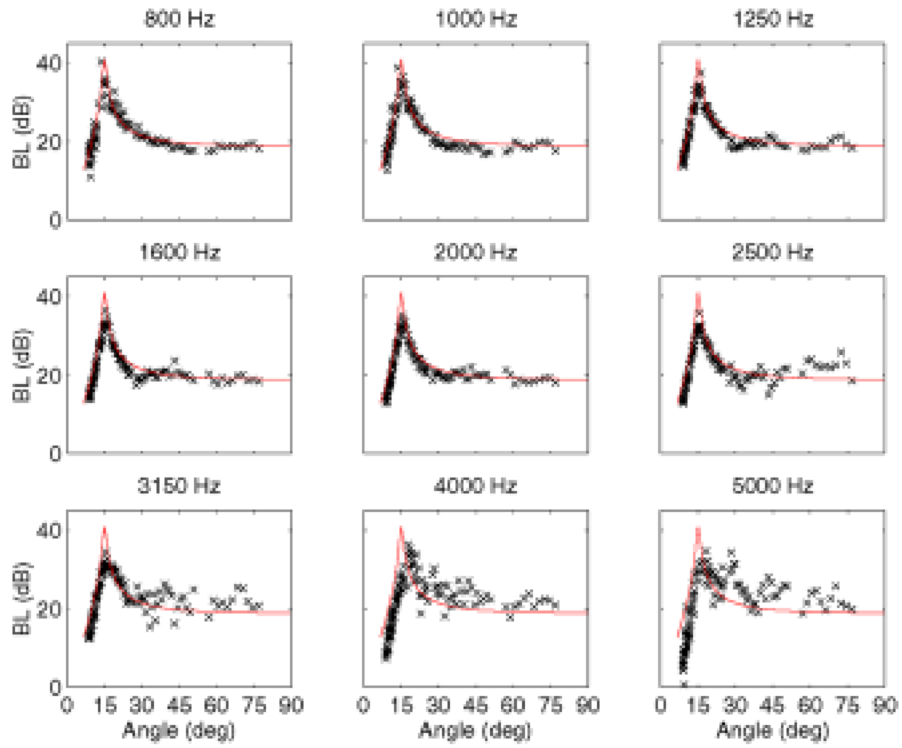

Fig. 11. Measured 1/3 octave bottom reflection loss (x) from the water–sediment interface of Site 4 with the model results from the geoacoustic inversion (red line).

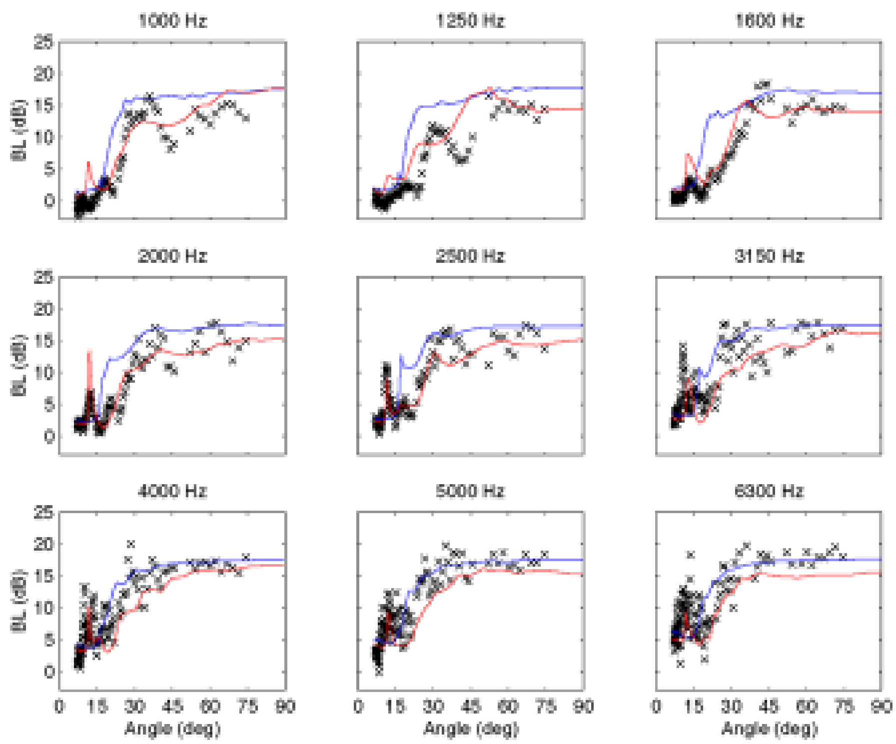

Fig. 12. Site 4 bottom reflection loss data (x) compared with model results using the time-domain (blue) and modified time-domain geoacoustic properties (red).

flection loss at the angle of intromission without resorting to unrealistically large attenuation values.

The reflection loss data for the upper 20 m of the sediment column are shown in Fig. 12. Also shown are the predictions using the geoacoustic properties derived from the time domain data (blue line). The model fits the measurements in a general sense, but there are clues in the reflection data that can improve the geoacoustic model. For example, using the apparent critical

TABLE I
GEOACOUSTIC PROPERTIES FOR SITE 4

Thick-ness (m)	Sound Speed (m/s)	Density (g/cm^3)	Attenuation (dB/m/kHz)
8.4	1490.	1.32-1.5	0.01
0.2	1550	1.7	0.05
1.6	1490.	1.6	0.02
0.8	1660	1.80	0.2
-	1615	1.70	0.05

angle of the data (~25 degrees) the second layer sound speed was estimated at 1660 m/s. Also, the peak in the reflection coefficient at about 13 degrees (2–3 kHz) confirms the existence of, and provides estimates of the properties for the high-speed layer at 8.4 m. The reflection predictions (Fig. 12 red line) using the modified geoacoustic properties [see Fig. 10(b)] are in better agreement across angle and frequency. It is believed that scattering from the layer at 10 m subbottom explains why the data have a generally higher loss than the model at high frequencies. Note also that there is greater variability in the high-frequency data, which may be indicative of scattering.

Including the sound speed gradient in the first sediment layer has a negligible effect on the reflectivity and so for simplicity was not included in the geoacoustic properties. The accompanying density gradient can not be ignored; it has the effect of changing the impedance contrast at the base of the silty-clay layer. The fine-scale layering properties (see the Appendix) had a minor influence on the reflection coefficient integrated over the upper 20 m and thus were not included. The geoacoustic properties for Site 4 are given in Table I. The basement attenuation value has considerable uncertainty, since the reflection loss is not sensitive to that parameter. The basement parameter was set from scattering analyses in the next section.

C. Site 1 Reflection Analysis

Site 1 time series reflection data (Fig. 13) are similar to Site 4 in that the water–sediment interface reflection apparent at 0.0095 s^2 is weak relative to the following reflections. At Site 1, two strong reflectors follow very close in time after the water–sediment interface at about 0.0099 s^2 and 0.0101 s^2. No other reflecting horizons[2] are apparent until about 30 m subbottom (not shown) where there is a relatively weak low-frequency (below 1 kHz) reflector.

The sediment sound speed profile obtained from the time domain analysis in the upper few meters is shown in Fig. 14. Note that the first layer sound speed is essentially identical to that at Site 4. Due to the closely spaced subbottom layers, it was difficult to accurately pick the hyperbolae for the second layer. However, the frequency-domain data (reflection loss) provide information on this layer.

Processing the reflection coefficient in individual layers was not possible at this site due to the close spacing of the layers near the interface, and layers below a few meters do not contribute to the reflection coefficient at these frequencies. The measured total energy reflection loss (x) at this site is shown in Fig. 15. The blue curve shows the predictions using the sound speed profile from Fig. 14(a) which do not agree particularly well with the measurements (almost certainly due to inaccuracies in the second layer sound speed). Using the location of the critical angle at high frequency (5 kHz) as a guide, the sound speed of the second layer was estimated to be 1780 m/s. Oscillations observed in the high angle (>45 degrees) and 1–2 kHz data suggested that the second layer thickness was about a factor of 2 too large. The modified sound speed profile [red dashed curve of Fig. 14(b)] fits the measured reflection data considerably better (see the red curve in Fig. 15).

However, the fit to the low angle data in Fig. 15 requires an unrealistically large attenuation of 0.1 dB/m/kHz in the first (silty-clay) layer. It is unrealistic from the standpoint that it is a factor of 10 higher than the first layer attenuation at Site 4 (which has the same sound speed); it is greater than the effective attenuation from the similar sediment type at Site 4, and higher than that found in the literature ([16]–[18], [7] or even [15]) would predict for a silty clay. In connection with this, note that the predictions do not match the data at high-frequency (4–6 kHz) high angle (>45 degrees) and the bias in the model versus the data increases with increasing frequency. A probable explanation for both these effects is scattering due the large inclusions as shown in Fig. 5.

In order to estimate the effect of scattering in the second layer, several model predictions were made including scattering at the second layer interface (using the Kirchhoff approximation as implemented in OASES [19] reflection module). Fig. 16 compares the smooth layer (red) with an rms roughness of 3.5 cm (blue); both predictions use the same attenuation found at Site 4 (0.01 dB/m/kHz). The frequency dependence of the low and high angle predictions indicates that scattering plays an important role in the reflection process. However, noting the different low-angle (<30 degrees) dependence of the model and data at 5–6 kHz, volume scattering rather than interface scattering may be the actual mechanism involved. Table II provides the geoacoustic properties at this site.

D. Summary of Reflection Results

In summary, the western Malta plateau appears to have a blanket of surficial silty clay with uniform geoacoustic properties but spatially variable thickness. The thickness decreases seaward (see Fig. 2). Below the silty-clay layer there are several thin (tens of centimeters) high-speed layers. Below the thin layers, there is a thick layer of 1600 m/s that effectively forms the acoustic basement at these frequencies. From the core data at Site 1, this sandy layer has large inclusions of shells, shell fragments, and pebbles. The high compressional speed layer may also have large inclusions. There appears to be significant scattering at this layer, especially apparent at Site 1. There is no independent data to indicate that the inclusions also exist at Site 4; however, this seems to be implied inasmuch as the velocity of that layer is almost identical (less than 1% difference between the two sites). Analysis of the reflection data provide sound speed, density, attenuation and layer thickness estimates of the sedimentary structure required for scattering predictions.

[2]The feature on the positive ranges at about 0.0105 s^2 and 400 m offset is a reflection from the tow ship and not a sediment reflector.

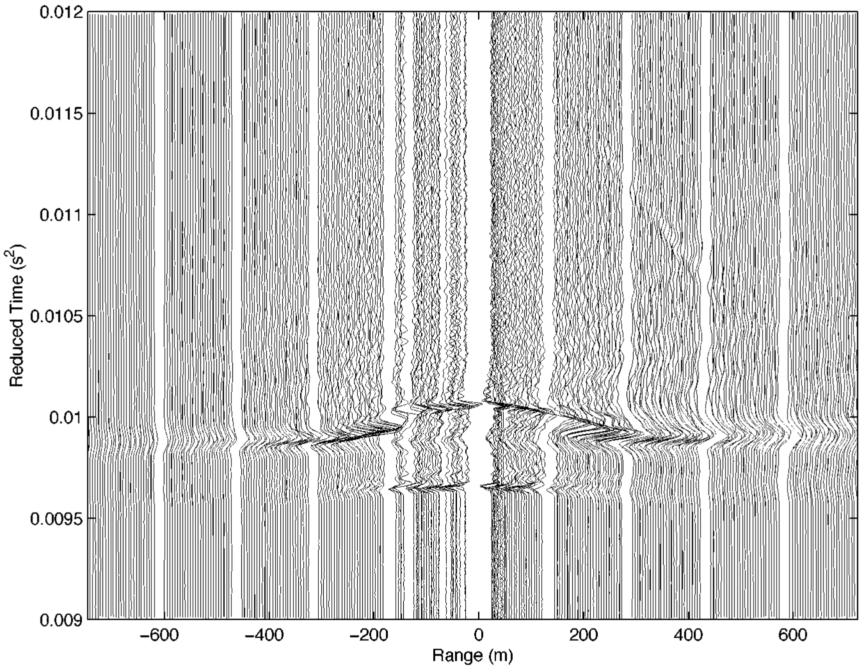

Fig. 13. Broadband reflection time series data at Site 1 with a reducing velocity of 1512.8 m/s. The water–sediment interface reflection is at 0.0095 s^2.

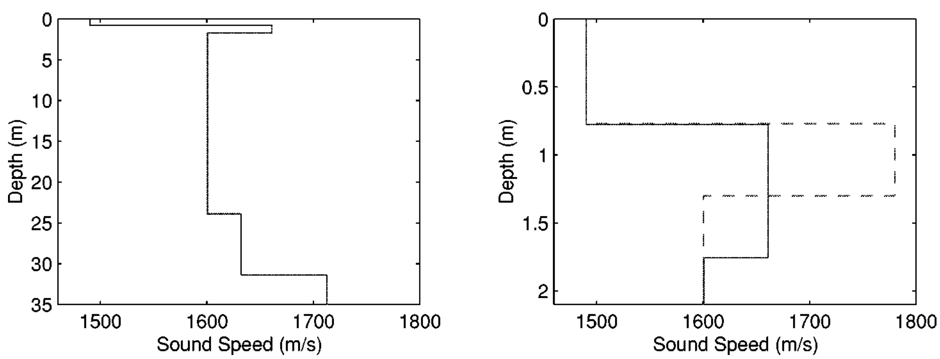

Fig. 14. Sediment sound speed profile at Site 1. The solid curve is from the time-domain analysis, the dashed line is from the frequency-domain (reflection analysis).

IV. Scattering Measurements

In this section, bottom scattering measurements are presented and interpreted in light of the geoacoustic properties obtained from the reflection analysis.

A. Measurement Technique Overview

Like the reflection technique, the scattering measurements are "local," i.e., yield scattering strength in a relatively small (several 100 m) radius. The technique allows not only measurement of bottom scattering strength but also provides information on the scattering mechanism (i.e., interface or subbottom volume scattering). Knowledge of the scattering mechanism is important because it can serve as a key for predicting the frequency dependence of the scattering. Details of the measurement and analysis technique are given in [20].

The scattering mechanism information is contained in the beam time series. Figs. 17 and 18 show the various multipath orders and the resulting arrival structure. The beam spacing in Fig. 18 is consistent with a Hanning-shaded 32-element array at 0.18-m spacing at 3600 Hz. This paper will focus on backscattering, branch a. Deviations from the predicted arrival structure of branch a, including time delays, arrival elongation, or the addition of other branches directly point to the existence of subbottom scattering.

In the following sections, an overview of the scattering model is first given. Then, following a brief analysis of the beam time series data, the scattering strength data and model results are presented and discussed.

B. Scattering Modeling Overview

For analysis of the bottom scattering data, the model of [7] is employed, which departs from most other bottom scatter models in that it computes received level in the time domain from the sediment/basement interfaces and a distribution of subbottom scatterers, then processes the data for scattering strength using the same assumptions employed in the data processing. The importance of the approach is that it provides a result that is directly comparable with measured data. Some subbottom scattering models (e.g., that compute the scattering strength in the

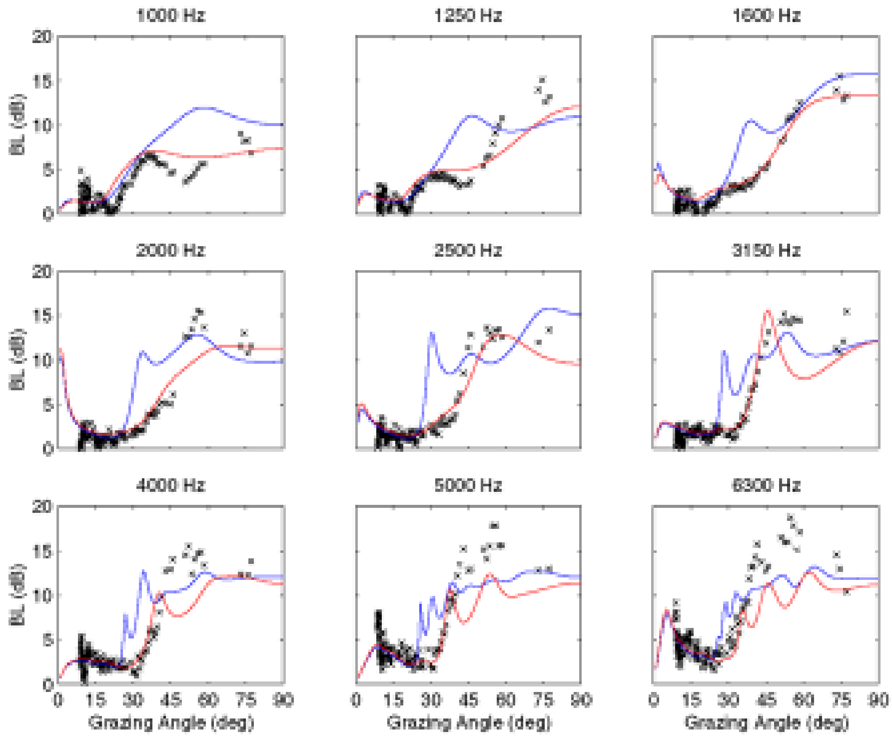

Fig. 15. Comparison of Site 1 measured reflection loss (x) with model using layer structure from the time-domain analysis (blue) and the modified time-domain analysis (red).

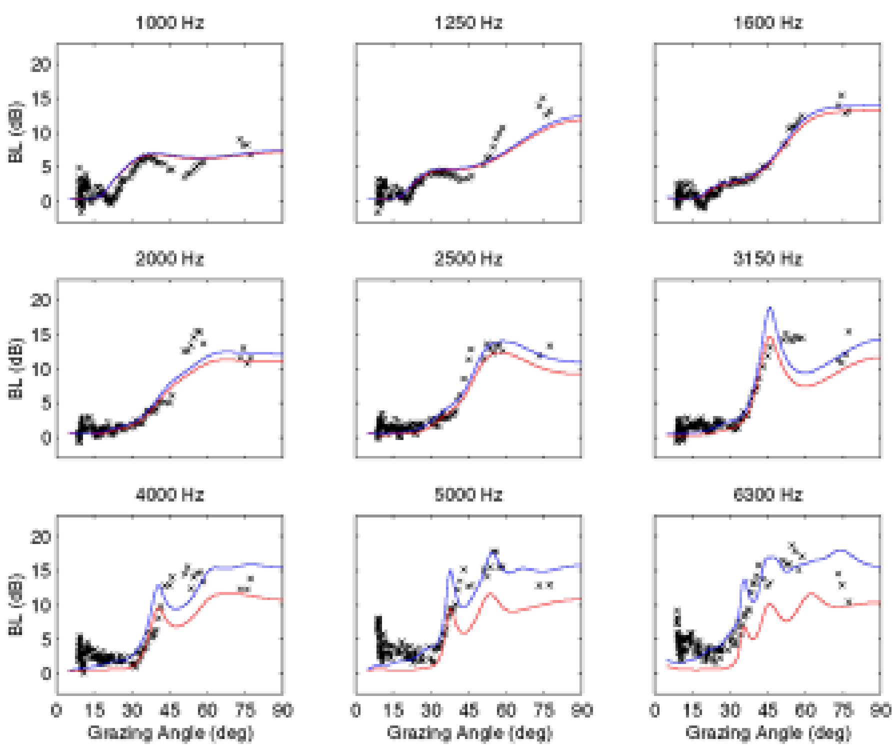

Fig. 16. Comparison of Site 1 measured reflection loss (x) with model using geoacoustic properties from Table II with roughness (blue) and without roughness (red).

frequency domain) do not account for the time-angle artifacts that exist in measured data when subbottom scattering plays a significant role. These artifacts exist because 1) the frequently employed local-plane wave approximation breaks down for the experimental geometries and 2) the bottom scatter data processing corrects for insonified area at the water–sediment and not for insonified volume or insonified area at a subbottom layer horizon.

The model considers a refracting sediment layer over a half-space and treats scattering from the water–sediment interface,

TABLE II
GEOACOUSTIC PROPERTIES FOR SITE 1

Thick-ness (m)	Sound Speed (m/s)	Density at top (g/cm^3)	Attenuation (dB/m/kHz)	RMS roughness (cm)
0.8	1490.	1.32	0.01	0
0.5	1780	1.85	0.2	3.5
-	1600	1.62	0.05	--

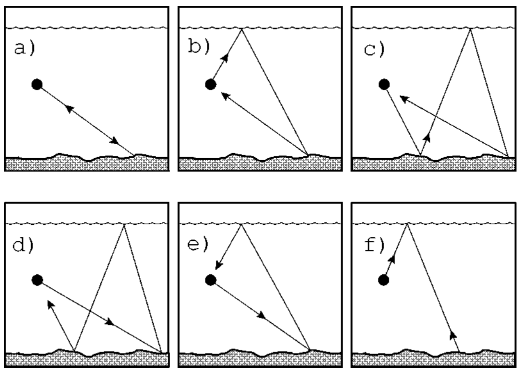

Fig. 17. Bottom scattering multipaths.

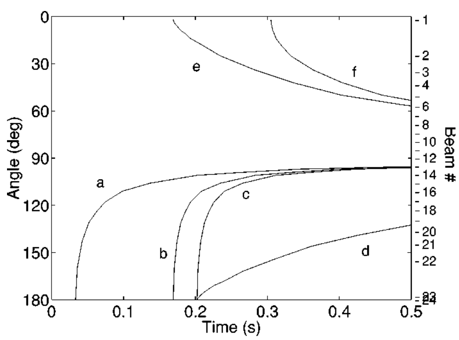

Fig. 18. Vertical arrival structure for multipaths of Fig. 17. 180° is toward seafloor.

scattering from within the sediment layer, and scattering from the basement interface. The received level is computed in the Born approximation as a sum of delayed, scaled, replicas of the transmit source intensity $S(t)$ as

$$RL(t;\,\theta) = 10\log\left[r_o^{-2}\sum_{k=1}^{2}\sum_{i=1}^{N} S(t-t_i)\zeta_{i,k}^{\mathrm{in}}\zeta_{i,k}^{\mathrm{out}}\sigma_k(\theta_{i,k}^{\mathrm{in}},\,\theta_{i,k}^{\mathrm{out}})A + r_o^{-2}\sum_{j=1}^{M} S(t-t_j)\zeta_j^{\mathrm{in}}\zeta_j^{\mathrm{out}}\frac{dP}{d\Omega}(\theta_j^{\mathrm{in}},\,\theta_j^{\mathrm{out}})\right] \quad (3)$$

where $r_o = 1$ m is the unit distance, k is the index for the interface, ζ_i^{in} and ζ_i^{out} are the intensity transmission ratios (including the beam pattern) from the source to scattering cell i and from cell i back to the receiver, respectively, σ is the scattering kernel, and A is the area of the cell. The scattering kernel for the interfaces uses a two parameter (spectral strength, β and exponent, γ of the roughness spectrum), power law model [21]. For subbottom volume scattering $dP/d\Omega$ is the differential scattering cross-section and following [6] requires 3 inputs: spectral intensity I, spectral exponent η, and aspect ratio Λ of the velocity fluctuations. The dip angle is assumed to be 0 and the grain density $= 2.65$ g/cm^3.

Despite the fact that the model includes all of the generic scattering mechanisms, the environment in the study area is more complex than the model considers. For example, the model only allows one layer between the water–sediment interface and the basement; both Site 1 and Site 4 have more than one layer. Also, the model only allows volume scattering within the single sediment layer, whereas at the Sites in the study area, volume scattering (if important) occurs in sediment layers below the first layer. As an interim measure, several approximations were introduced to estimate these effects. In order to approximate the effect of multiple layers between the water–sediment interface and the basement, the scattering kernel was multiplied by the two-way transmission coefficient as computed by OASES [19]. In order to approximate the effect of multiple layers between the water–sediment interface and deeper volume scatterers bounded with an upper depth $z = h$, the ratio of the received intensity for interface scattering at h, to that at the sediment interface was multiplied by the received intensity for volume scattering at $z = 0$. However, the conclusion is that the layering observed in the study area underscores the need for more complex models that incorporate these environmental effects properly and are able to directly model real data.

For the model used in this study, ray theory [22] was used to compute the transmission loss ($10\log\zeta$) terms, the range step was set to 0.5 m, and the grid was based on polar coordinates around the receiver position. Volume scattering was computed with a depth spacing of 1 m. Contributions from the direct blast and the normal incidence air–sea reflection were not included in the calculations. Source levels and beam patterns were computed based on calibration results [20].

C. Site 10 Beam Time Series

Site 10 is on the eastern edge of the Malta Plateau, just 1.5 km west of the Ragusa ridge, with a water depth of 126 m. This site was selected to examine the difference in scattering between the central Plateau (Site 1) and its eastern edge. The center of the receive array was 22 m above the bottom.

The beam time series data are shown in Fig. 19 along with modeled arrival branches (white dashed lines) whose geometrical meaning can be understood from Figs. 17 and 18. The scattering branch that does not correspond to a modeled arrival (commencing at 0.14 s on beam 0) is simply monostatic scattering from the sea surface.

Note that there is no time delay between the modeled and measured scattering branch a; moreover, modeling (not shown) indicates that there is no substantial time spreading of this branch. These two facts indicate that the scattering is coming from the upper 10 m of sediment (i.e., the limits of the pulse/beam resolution). The core data show a high-speed sandy gravel layer ~60 cm subbottom. This layer is probably the dominant mechanism giving rise to the scattering.

D. Site 4 Beam Time Series

Site 4 is in 102 m water depth at the northern edge of the study area. The center of the receive array was 29 m above the bottom.

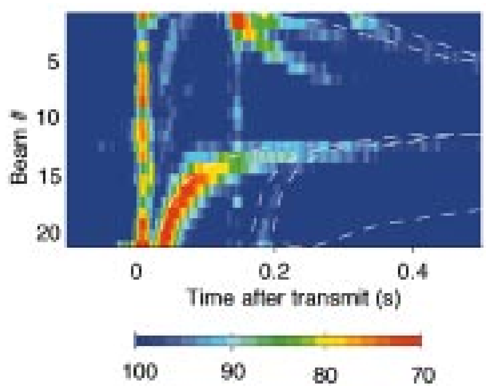

Fig. 19. Averaged (10 pings) beam time series from 3600-Hz bottom scattering at Site 10. The processing bandwidth is 150 Hz. The quantity plotted is received level re 1 μPa^2/s/Hz. The direct blast is seen just after 0 s across all the beams and the surface reflection is observed at 0.14 s. The vertical white dashed line at 0.14 s is the model result for the surface reflection; the other white dashed lines are model results for the various bottom scattering paths. No delay between the modeled and measured arrivals is observed indicating that the scattering is coming from at or near the sediment surface.

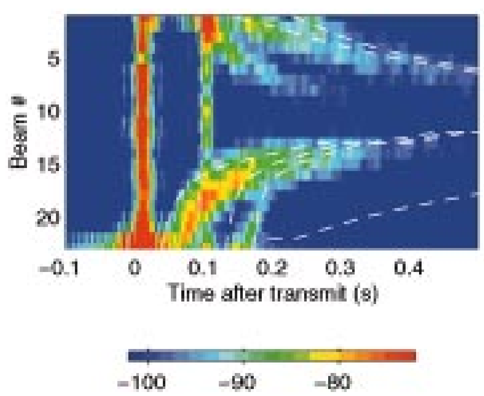

Fig. 20. Averaged (10 pings) beam time series from 3600-Hz bottom scattering at Site 4. The delay between the modeled and measured arrivals indicates that the scattering comes from about 10 m below the water–sediment interface. This depth corresponds with the layer horizon observed in the reflection data (see Fig. 10).

The reflection analysis at Site 4 shows that the upper 10 m of sediment is silty clay with a sound speed less than that of the overlying water column. As will be shown, the presence of the surficial silty-clay layer has an important effect on the scattering as well as on the reflection.

Fig. 20 shows the beam time series from the bottom scattering measurement. The predicted backscattering branch (white dashed curve) commences 0.04 s past the direct blast at normal incidence (beam 23). The measured backscattering branch (branch a in Figs. 17 and 18) arrives substantially later than the prediction. This time delay, $\sim$14 ms, indicates that the scattering is coming not from the water–sediment interface, but rather from a horizon about 10 m subbottom.

The time delay is more clearly observed on bistatic branch b in beams 18–23. The first branch b arrival, denoted branch b', visible at 0.15 s on beam 23, is the normal incidence reflection from the water–sediment interface. Fourteen milliseconds later on the same beam (immediately preceding branch c) there is another arrival, branch b'', that corresponds to a reflection arrival

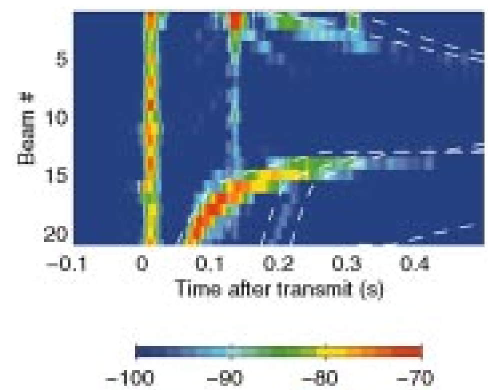

Fig. 21. Averaged (10 pings) beam time series from 3600-Hz bottom scattering at Site 1. No delay between the modeled and measured arrivals is observed indicating that the scattering is coming from at or near the sediment surface.

from 10 m subbottom. It is significant to observe that scattering branch b' from the water–sediment interface decays rapidly for angles below normal incidence; below 55° (beam 21), the water–sediment interface scattering branch b' is about 10 dB less than that from branch b''. These data provide direct proof (without modeling assumptions) that the dominant scattering mechanism in this environment is subbottom, not water–sediment interface, scattering. The comparison between interface and subbottom scattering is more easily observed on branch b than branch a because the latter is contaminated by array overload (clipping) from the direct blast.

From the reflection analysis it is known that the first significant subbottom layers (in terms of impedance contrast) occur at about 10 m subbottom (see Figs. 8 and 10 and Table I). The scattering data indicate it is that horizon that is the dominant scattering mechanism. Thus, the reflection data not only corroborate features observed in the scattering data, but also provide quantitative sediment properties required for physics-based modeling. It is this utility of the coupled measurement concept that is one of the central points of the paper, i.e., that reflection data can provide key information required for interpreting the scattering measurements.

E. Site 1 Beam Time Series

Site 1 is in 128 m water depth near the center of the study area. The center of the receive array was 29 m above the bottom. Reflection analysis at Site 1 showed a strongly reflecting/scattering layer 0.8 m below the water–sediment interface. In agreement with that analysis, the beam time series at Site 1 (Fig. 21) show no measurable[3] time delay between the modeled and measured scattering arrivals.

F. Scattering Strength Analysis

Bottom backscattering strength can be extracted from the beam time series following [20]. In modeling the data, the deterministic geoacoustic properties (i.e., layer thicknesses, sound speeds, densities, attenuations) obtained from the reflection analysis in the previous section are used. The reflection

[3]The uncertainties associated with the source depth, receiver depth, and water depth are of order a meter, i.e., insufficient for determining departures from the predicted arrival structure of that order.

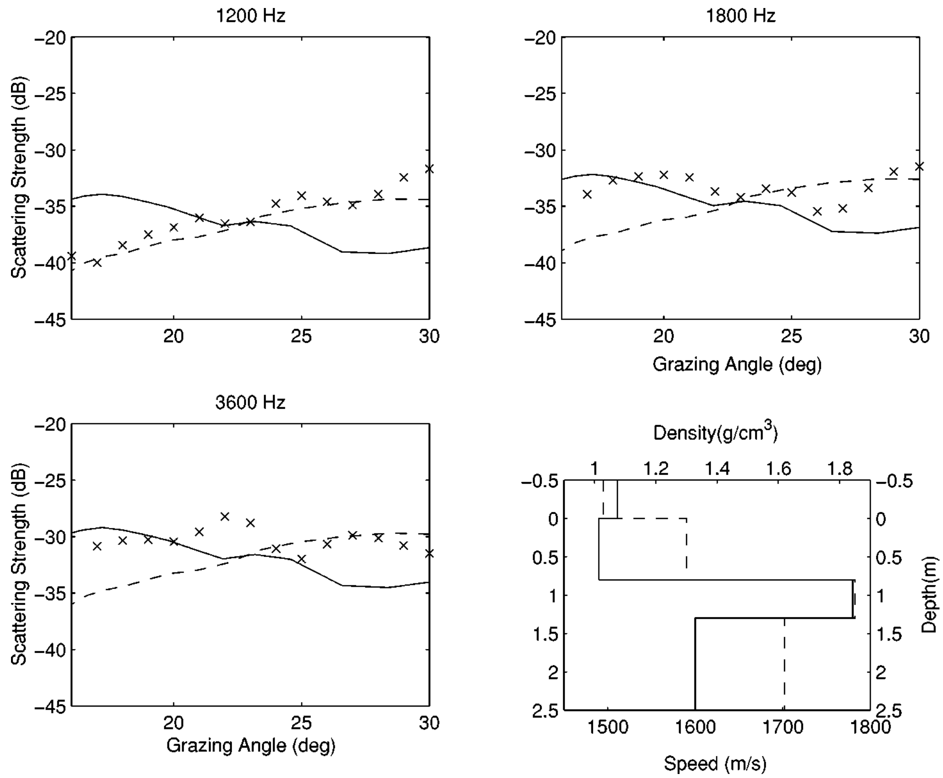

Fig. 22. Measured (x) scattering strength at Site 1 with model predictions, from 0.8 m subbottom (dashed line) and from 1.3 m subbottom (solid line). The layering structure is shown in the bottom left panel, density is the dashed line.

analysis also provided clues about dominant scattering mechanisms, i.e., that the water–sediment interface impedance was low enough so that scattering from it would almost certainly be negligible, and that the subbottom layers with a high impedance were the probable mechanism for scattering. The time series analysis appeared to confirm this. Furthermore, the scattering strength model was run with roughness parameters reasonable for the silty-clay boundary ($\beta = 1.0 \times 10^{-5}$ m^4 and $\gamma = 3$) that gave predictions 15–20 dB lower than the measurements, thus indicating that the interface plays a negligible role in the scattering process.

Scattering strength (x) as a function of angle and frequency at Site 1 are shown in Fig. 22. The data were averaged over 10 pings and a 2 degree sliding window, the standard deviation of the data is about 3 dB. In order to fit the model to the data in Fig. 22, the basement spectral strength and exponent were varied. The angular dependence in the model predictions are controlled almost entirely by the layer densities and sound speeds, which were fixed in the reflection analysis. Changing the spectral strength changes only the overall amplitude; changing the exponent modifies the frequency dependence. The dashed curve represents the geoacoustic parameters of Table II with $\beta = 3.0 \times 10^{-5}$ m^4 and $\gamma = 3$. The two model results reasonably match the data except at the low angles at 1800 Hz and 3600 Hz. The solid curve, representing scattering at the basement interface (but excluding the effect of the 0.5 m high-speed layer), used $\beta = 1.2 \times 10^{-4}$ m^4 and $\gamma = 3$ and appears to better explain the 1800 Hz and 3600-Hz low angle data.

Site 4 is landward about 11 km and differs ostensibly from Site 1 in the thickness of the silty-clay layer. While the sound speed of the basement was comparable at the two sites, it was not known if the scattering characteristics were also similar. Fig. 23 shows the measured data with modeling results assuming the same scattering parameters at the basement interface as at Site 1 (solid curve). This assumption appears to be suitable at 3600 Hz. Note that the 3600 Hz measured and modeled Site 1 scattering are about 5 dB higher than at Site 4. This is due to two effects: 1) differences of the thickness of the silty-clay layer and 2) the presence of the thin layer at Site 4 at 8 m subbottom.

The Site 4 angular dependence at 1800 and 1200 Hz is quite different from that at 3600 Hz. The rapid decrease with angle could be explained by either scattering from an interface of $>$1800 m/s or scattering from within the basement volume. The reflection analysis appears to discount the former so the latter seems to be more reasonable. The dashed curves in Fig. 23 were computed with sediment volume parameters of: $I = 3.8 \times 10^{-3}$ m$^{-0.8}$, $\eta = 1.8$ and $\Lambda = 4$. The overall frequency and angular dependence indicates that volume scattering plays a role at frequencies below 3600 Hz and at 3600 Hz for angles above 25 degrees. The fit was also dependent upon attenuation (0.05 dB/m/kHz was used) in the basement layer This deterministic property was allowed to vary inasmuch as it was not well constrained by the reflection analysis.

Measured data at Site 10 are shown in Fig. 24. Since there were no reflection data at this site, and core data showed a similar structure to Site 1, the Site 1 layering and scattering parameters were employed. The scattering strength at the higher two frequencies is quite similar with Site 1. The reason for the rapid decrease in scattering strength versus angle at 1200 Hz may be

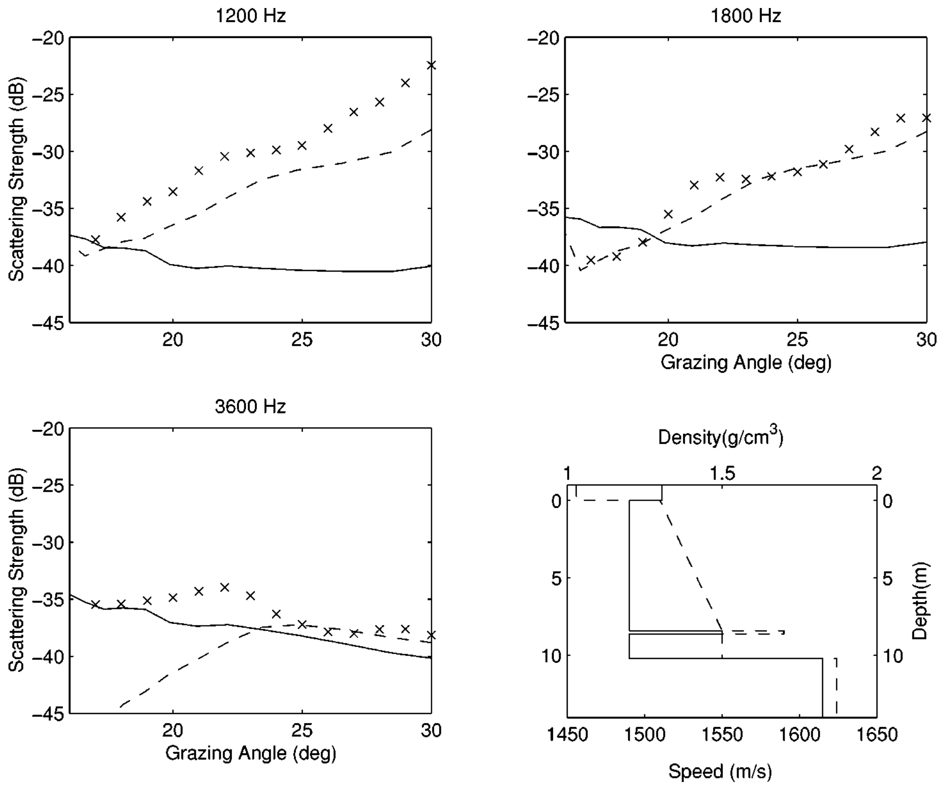

Fig. 23. Measured (x) scattering strength at Site 4 with model predictions for interface scattering at 10 m subbottom (solid line) and volume scattering from 10 to 24 m subbottom (dashed line). Comparison with Site 1 at 3600 Hz, shows about a 5-dB decrease in scattering strength.

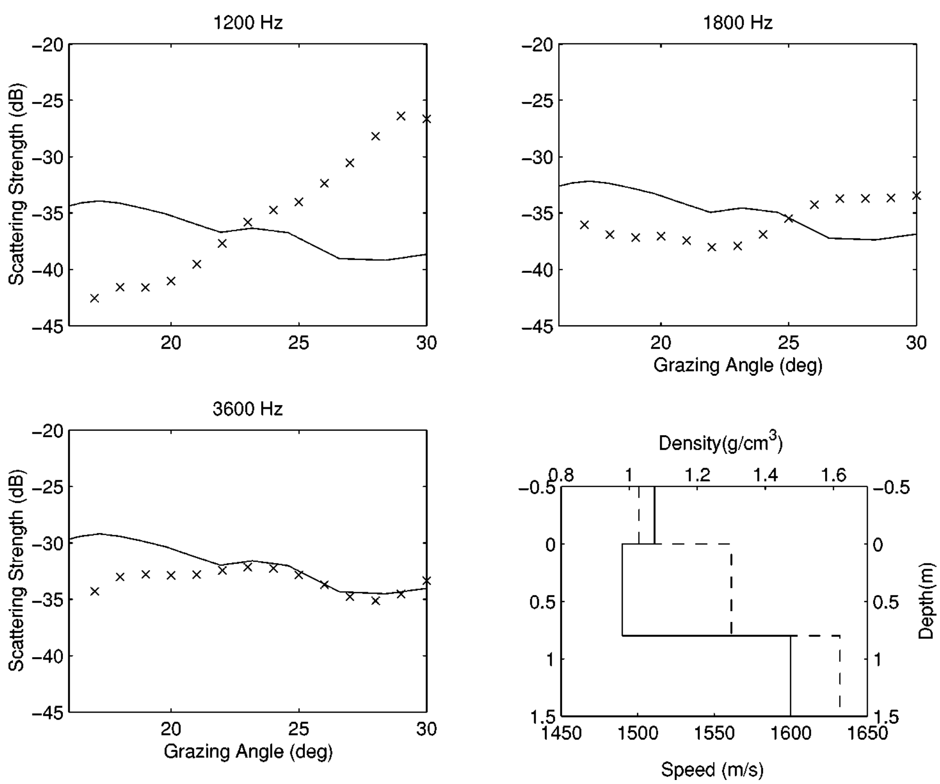

Fig. 24. Measured (x) and modeled (solid line) bottom scattering strength at Site 10. The layering structure shown in the bottom left panel as well as the scattering parameters were taken from Site 1. Comparison with Site 1 shows similar scattering strength at 1800 and 3600 Hz. The scattering at 1200 Hz may be governed by volume scattering.

due to volume scattering given the similarity in the angular dependence with Site 4.

In terms of regional characteristics, the 3600-Hz data are congruous with subbottom scattering from the basement interface

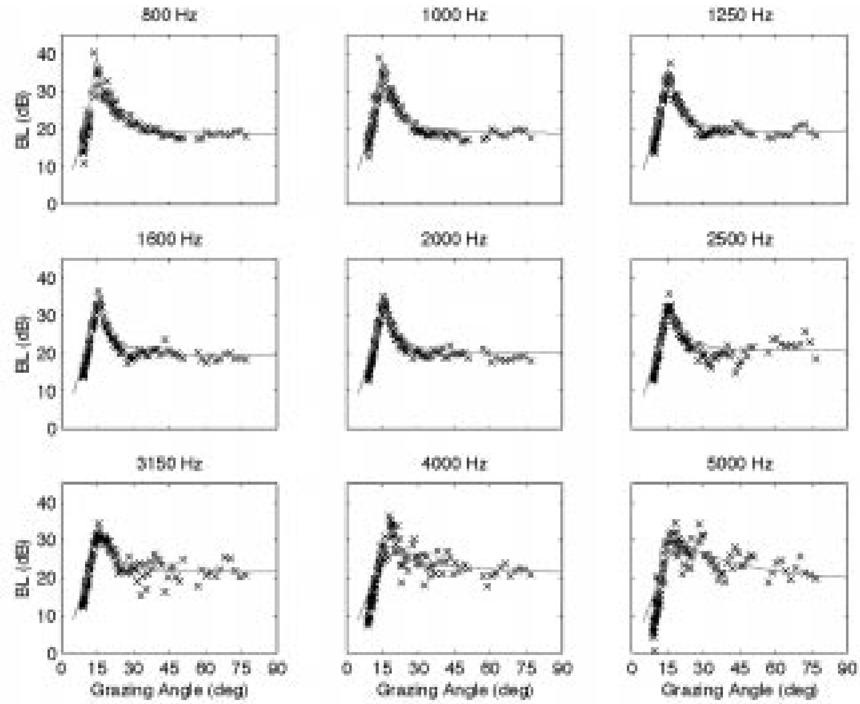

Fig. 25. Measured reflection loss (x) with the model including a 10-cm surface layer. Note the shift in the modeled angle of intromission at high frequencies that is consistent with the data. Note also the improved fit of the high angle data relative that of Fig. 8.

with consistent values at all three sites ($\beta = 1.2 \times 10^{-4}$ m^4 and $\gamma = 3$). At lower frequencies the situation appears more complex, or at least is not fully explained with the present level of modeling. The 1800-Hz data seems to be consistent between Sites 1 and 10 with the same parameters as at 3600 Hz ($\beta = 1.2 \times 10^{-4}$ m^4 and $\gamma = 3$), however at 1800 Hz and below at Site 4, the dominant scattering mechanism appears to be the basement volume.

One conclusion is that more complex models of acoustic scattering are required. On the other hand, it might be argued that the data could be fit with simpler models, i.e., the scattering mechanism could be ignored and the data fit with an interface scattering model. However, this alternative leads to an inability to extrapolate the data in space or frequency and therefore makes interpreting regional variability difficult. It is believed that complexity in the models (sufficient to capture the principal mechanisms) will simplify regional modeling of scattering strength. As an example, the thickness of the overlying silt-clay layer has a definite measurable impact on the scattering strength. This effect can be relatively easily treated in physics-based modeling, whereas trying to predict the effect heuristically, i.e., with an interface scattering model would be cumbersome at best.

V. Summary and Conclusion

In studies of acoustic interaction with the seabed, sometimes only the quantity of immediate interest (reflection or scattering) is measured. Measuring both quantities in a coupled technique allows a more complete and self-consistent characterization of the seafloor geoacoustic properties and their site-to-site variability.

The coupled analysis provided substantial detail about the mechanisms involved in both the reflection and scattering. Acoustic interaction with the seafloor on the Malta Plateau is dominated by reflection and scattering from the subbottom rather than the sediment interface. The first sediment layer (silty clay) is nearly acoustically transparent and contributes very little to the reflection and scattering process, except as a lens, modifying the angular content of the incident field on the subbottom layers. It appears to have uniform geoacoustic properties across the plateau, but variable thickness, roughly 1–10 m. The dominant scattering mechanism at Sites 1, 4, and 10 appear to be the layer between 155–165 ms two-way travel at Site 4 (0 range) in Fig. 2. At Site 4, there is evidence that 3600-Hz scattering is generated in this layer, which is 10 meters (greater than 20 wavelengths) below the seafloor.

Appendix
Effect of Fine-Scale Layering on the Angle of Intromission

In Fig. 11, it was observed that the halfspace model did not fit the measured reflection loss data above 2 kHz. In this appendix, an explanation is advanced assuming the presence of fine-scale layering.

Note that at 4–5 kHz (Fig. 11) the low angle data (below the angle of intromission) are shifted to higher angles relative to the halfspace predictions. This indicated that the high frequencies "see" a lower sound speed and/or density than the low frequencies. The simples explanation is that there is a surficial layer with a lower sound speed. Note also, that at high frequencies, the high angle (>45 degrees) reflection data have a higher loss than the low frequencies, which is also consistent with a surface layer of lower sound speed and density.

Fig. 25 shows the data predictions using a 10-cm surficial layer of 1470 m/s, 1.28 g/cm^3 and 0.01 dB/m/kHz (see Table III). The presence of this layer seems to explain: 1) the increase in reflection at high frequencies; 2) the increase of the angle of intromission with increasing frequency; and 3) the

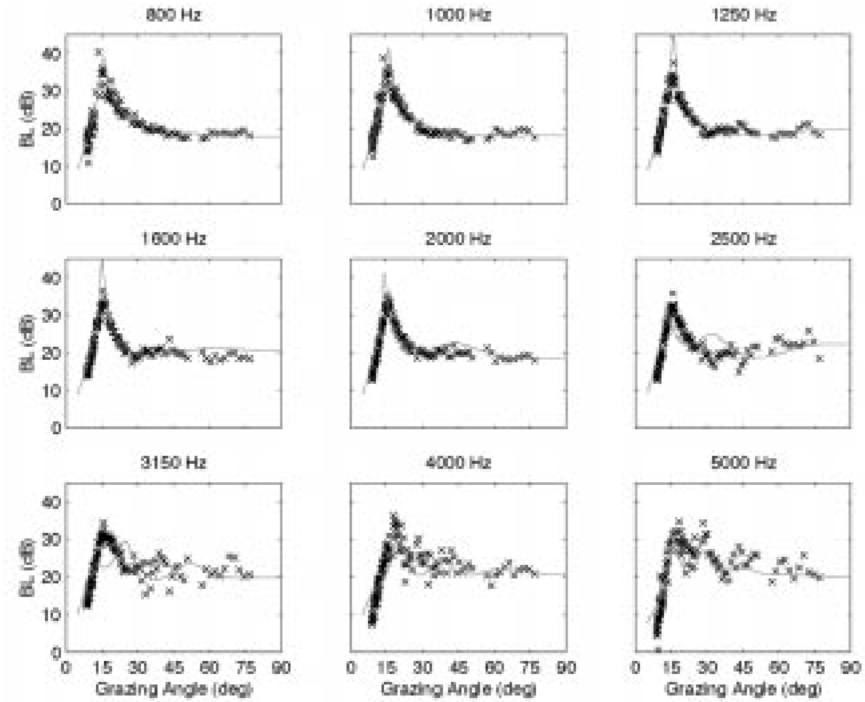

Fig. 26. Measured reflection loss (x) with model including fine-scale near surface layering. Note that the oscillation structure in the model is similar to that in the data, indicating that the data oscillations are probably a resonance due to fine-scale layering.

TABLE III
GEOACOUSTIC PROPERTIES FOR FIG. 25

Thick-ness (m)	Sound Speed (m/s)	Density (g/cm^3)	Attenuation (dB/m/kHz)
0.10	1470.	1.28	0.01
--	1480.	1.32	0.01

TABLE IV
GEOACOUSTIC PROPERTIES FOR FIG. 26

Thick-ness (m)	Sound Speed (m/s)	Density (g/cm^3)	Attenuation (dB/m/kHz)
0.10	1470.	1.28	0.01
0.50	1480.	1.32	0.01
0.07	1470.	1.28	0.01
--	1480.	1.32	0.01

reflection loss at the angle of intromission without resorting to large attenuations. The one aspect it does not explain is the presence of oscillations in the data above the angle of intromission, e.g., apparent at 5 kHz from 2 to 60 degrees.

The oscillations at 4–5 kHz are presumed to come from layering. Fig. 26 shows the predictions using a three-layered bottom of Table IV. Note that, at 5 kHz, the predicted oscillations agree reasonably well with the measured data. While the oscillations do not perfectly match the data, the similarity of the predicted oscillatory structure to that measured give credence to the hypotheses that fine-scale layering:

- is responsible for the high-frequency departure form the half-space predictions;
- controls the reflection loss at the angle of intromission.

ACKNOWLEDGMENT

The author would like to thank the scientific staff and captain aboard the NATO R/V Alliance during the cruises in which these data were collected. Special thanks to J. Osler who developed the software for the time domain inversion of the reflection data and to Piero Boni who managed the data acquisition with energy and expertness.

REFERENCES

[1] A. N. Ivakin, “Sound scattering by random inhomogeneities in stratified ocean sediments,” *Sov. Phys. Acoust.*, vol. 32, no. 11, pp. 492–496, 1986.
[2] P. C. Hines, “Theoretical model of acoustic backscatter from a smooth seabed,” *J. Acoust. Soc. Amer.*, vol. 88, no. 7, pp. 324–334, 1990.
[3] D. J. Tang and G. V. Frisk, “Spectral parameterization of scattering from a random ocean bottom,” *J. Acoust. Soc. Amer.*, vol. 92, no. 11, pp. 2792–2799, 1992.
[4] A. P. Lyons, A. L. Anderson, and F. S. Dwan, “Acoustic scattering from the seafloor: Modeling and data comparison,” *J. Acoust. Soc. Amer.*, vol. 95, no. 5, pp. 2441–2451, 1994.
[5] P. D. Mourad and D. R. Jackson, “A model/data comparison for low frequency bottom backscatter,” *J. Acoust. Soc. Amer.*, vol. 94, no. 7, pp. 344–358, 1993.
[6] T. Yamamoto, “Acoustic scattering in the ocean from velocity and density fluctuations in the sediment,” *J. Acoust. Soc. Amer.*, vol. 99, no. 2, pp. 866–879, 1996.
[7] C. W. Holland and P. Neumann, “Sub-bottom scattering: A modeling approach,” *J. Acoust. Soc. Amer.*, vol. 104, no. 9, pp. 1363–1373, 1998.
[8] K. D. LePage and H. Schmidt, “Spectral integral representations of volume scattering in sediments in layered waveguides,” *J. Acoust. Soc. Amer.*, vol. 108, no. 10, pp. 1557–1567, 2000.
[9] M. D. Max and P. Colantoni, “Introduction: Geomorphological position and geology of the Sicilian–Tunisian platform,” *Unesco Reports in Marine Science*, vol. 58, pp. 1–2, 1993.
[10] C. W. Holland and J. Osler, “High resolution geoacoustic inversion in shallow water: A joint time and frequency domain technique,” *J. Acoust. Soc. Amer.*, vol. 107, no. 3, pp. 1263–1279, 2000.
[11] C. W. Holland, “Regional extension of geoacoustic data,” in *Proc. 5th Eur. Conf. Underwater Acoustics, ECUA’00*, Lyon, France, 2000, pp. 793–798.

[12] G. M. Bryan, “The hydrophone-pinger experiment,” *J. Acoust. Soc. Amer.*, vol. 68, pp. 1403–1408, Nov. 1980.
[13] J. Osler, “Unpublished manuscript,” SACLANT Undersea Research Centre.
[14] C. W. Holland, “Geoacoustic inversion for fine-grained sediments,” J. Acoust. Soc. Amer., vol. 111, pp. 1560–1564, 2002, to be published.
[15] E. L. Hamilton, “Geoacoustic modeling of the seafloor,” *J. Acoust. Soc. Amer.*, vol. 68, pp. 313–1339, 11 1980.
[16] S. K. Mitchell and K. Focke, “New measurements of compressional wave attenuation in deep ocean sediments,” *J. Acoust. Soc. Amer.*, vol. 67, no. 5, pp. 1582–1589, 1980.
[17] G. V. Frisk, J. A. Doutt, and E. E. Hayes, “Bottom Interaction of low-frequency acoustic signals at small grazing angles in the deep ocean,” *J. Acoust. Soc. Amer.*, vol. 69, no. 1, pp. 84–94, 1981.
[18] F. A. Bowles, “Observations on attenuation and shear-wave velocity in fine-grained marine sediments,” *J. Acoust. Soc. Amer.*, vol. 101, pp. 3385–3397, June 1997.
[19] H. Schmidt, “OASES version 2.2: User guide and reference manual,” Mass. Inst. Technol., 1999.
[20] C. W. Holland, R. Hollett, and L. Troiano, “A measurement technique for bottom scattering in shallow water,” *J. Acoust. Soc. Amer.*, vol. 108, no. 9, pp. 997–1011, 2000.
[21] D. R. Jackson, D. P. Winebrenner, and A. Ishimaru, “Application of the composite roughness model to high frequency bottom backscattering,” *J. Acoust. Soc. Amer.*, vol. 79, no. 5, pp. 1410–1422, 1986.
[22] E. K. Westwood and P. J. Vidmar, “Eigenray finding and time series simulation in layered bottom ocean,” *J. Acoust. Soc. Amer.*, vol. 81, no. 4, pp. 912–924, 1987.

Charles W. Holland received the B.S degree in mechanical engineering from the University of Hartford, Hartford, CT, in 1983 and the M.S. and Ph.D. degrees in acoustics from the Pennsylvania State University, State College, in 1985 and 1991, respectively.

From 1985 to 1987, and from 1989 to 1996, he was with Planning Systems Inc, McLean, VA, where he developed models for predicting acoustic interaction with the seabed. At the NATO SACLANT Undersea Research Centre in La Spezia, Italy, from 1996 to 2001, he developed new shallow-water measurement techniques for reflection and scattering from the seabed. He is presently a Senior Scientist at the Applied Research Laboratory of the Pennsylvania State University with research interests in seabed reflection and scattering and inversion of sediment geoacoustic properties.